

Electronic Energy Scales of CrX_3 ($X = \text{Cl}, \text{Br}, \text{and I}$) using High-resolution X-ray Scattering

Chamini Pathiraja,¹ Jayajeewana N. Ranhili,¹ Deniz Wong,²
Christian Schulz,² Yi-De Chuang,³ Yu-Cheng Shao,⁴ Di-Jing
Huang,⁴ Hsiao-Yu Huang,⁴ Amol Singh,⁴ and Byron Freelon¹

¹*Physics Department and Texas Center for Superconductivity,
University of Houston, Houston, TX 77204*

²*Helmholtz-Zentrum Berlin für Materialien und Energie, D-14109 Berlin, Germany*

³*Lawrence Berkeley National Laboratory, Berkeley, CA 94720*

⁴*National Synchrotron Radiation Research Center,
101 Hsin-Ann Road, Hsinchu Science Park, Hsinchu, Taiwan 30076*

(Dated: April 8, 2025)

Abstract

Chromium tri-halides CrX_3 ($X = \text{Cl}, \text{Br}, \text{and I}$) have recently become a focal point of research due to their intriguing low-temperature, layer-dependent magnetism that can be manipulated by an electric field. This makes them essential candidates for spintronics applications. These magnetic orders are often related to the electronic structure parameters, such as spin-orbit coupling (SOC), Hund's coupling (J_H), $p-d$ covalency, and inter-orbital Coulomb interactions. Accurately determining such parameters is paramount for understanding CrX_3 physics. We have used ultra high-resolution resonant inelastic x-ray scattering (RIXS) spectroscopy to study CrX_3 across phase transition temperatures. Ligand field multiplet calculations were used to determine the electronic structure parameters by incorporating the crystal field interactions in a distorted octahedral with C_3 symmetry. These methods provide the most detailed description of CrX_3 magneto-optical and electronic energetic (terms) to date. For the first time, the crystal field distortion parameters $D\sigma$ and $D\tau$ were calculated, and the energies of d orbitals have been reported. Our RIXS spectroscopic measurements reveal a clear energy separation between spin-allowed quartet states and spin-forbidden doublet states in CrX_3 . The role of SOC in Cr $2p$ orbitals for the spin-flip excitations has been demonstrated. The determined $10Dq$ values are in good agreement with the spectrochemical series, and Racah B follows the Nephelauxetic effect. Such precise measurements offer insights into the energy design of spintronic devices that utilize quantum state tuning within 2D magnetic materials.

I. INTRODUCTION

The chromium tri-halides CrX_3 ($X = \text{Cl}, \text{Br}, \text{and I}$) compounds have ferromagnetic (FM) order in the monolayer limit with Curie temperatures $T_c = 17 \text{ K}, 34 \text{ K}, \text{and } 61 \text{ K}$ for CrCl_3 , CrBr_3 , and CrI_3 , respectively [1–3]. The interlayer interactions in bulk CrCl_3 are antiferromagnetic (AFM), while CrBr_3 and CrI_3 exhibit FM order. The electronegativity between metal Cr and the halides decreases as the halogen changes from Cl to Br to I

[4, 5]. This results in increasing of $p-d$ covalency from CrCl_3 to CrI_3 . With the presence of spin-orbit coupling (SOC), the FM superexchange interaction across the $\sim 95^\circ$ Cr- X -Cr bonds becomes highly anisotropic in the edge-shared octahedral orientation in CrX_6 (see Fig. 1(a)) [6]. This magnetocrystalline anisotropy stabilizes the magnetic order in CrX_3 , overcoming the mermin-wagner theorem [7, 8], and leads to rich phase diagrams in CrX_3 . On the other hand, the magnetic ordering appears to be dependent

on the dimensionality, the atomic halogen constituents, layer interactions, and temperature. Understanding magnetism also appears to be linked to determining the electronic levels of chromium bands near the Fermi energy. These circumstances suggest that obtaining precisely determined energy scales is a prerequisite for constructing theoretical models that explain the magnetic ground states of CrX_3 . The development of a high-accuracy Hamiltonian for the CrX_3 , supported by experimental findings, is urgently needed to enhance the ability of the condensed matter physics community to deploy these intriguing materials. These findings could revolutionize the field of spin-based electronics since magnetism in CrX_3 compounds may be exploitable in the next generation of smart electronic devices, potentially surpassing the capabilities of graphene [9–15].

Spectroscopic measurements have been identified as an excellent technique for probing electronic transitions and determining the electronic structure of the transition metal (TM) halides. However, a significant challenge arises from dd electronic transitions being dipole forbidden [16, 17]. Even though some dd transitions may be observable using some optical spectroscopic techniques, electronic transitions with different spin multiplicities remain undetectable. This underscores the necessity for spectroscopic probes

that detect all potential dd transitions in order to determine a more accurate electronic structure in TM halides [18, 19]. With the development of synchrotrons, x-ray absorption spectroscopy (XAS), along with the resonant inelastic x-ray scattering (RIXS), has been used to probe the dd and charge-transfer (CT) excitations in TM complexes [20]. RIXS is a coherent photon-in/photon-out process. Together, XAS and RIXS methods allow detailed characterization of the bonding in TM compounds, and RIXS has been demonstrated to be a suitable tool for providing detailed electronic structure information in CrX_3 [21].

This paper reports enhanced RIXS spectral features in CrX_3 using ultra-high resolution spectroscopic instruments. A significant outcome of our study is the first experimental observation of a considerable energy separation between the spin-allowed quartet and spin-forbidden doublet states in multielectronic states in CrX_3 . The Tanabe-Sugano-like energy level diagrams (ELDs) have been calculated and compared with the experimental RIXS spectra to determine the energy scales, such as crystal field splitting and Racah parameters. Atomic multiplet $2p-3d$ RIXS calculations have been performed to reconstruct the experimental RIXS spectra, and the electronic structure parameters for different halide systems have been summa-

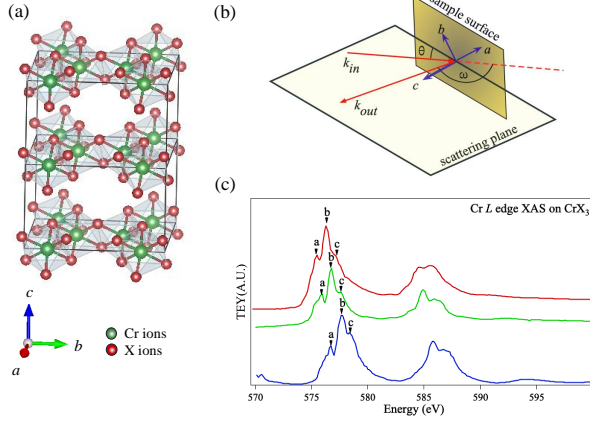


FIG. 1. (a) Lattice structure of CrX_3 . The metal Cr and halide ions ($X = \text{Cl}, \text{Br}, \text{and I}$) are shown in green and red, respectively. (b) The schematic diagram illustrates the experimental setup for RIXS measurements. k_{in} and k_{out} are the incident and scattered photon beam wave vectors. (c) Cr L -edge XAS measurements on CrX_3 ($X = \text{Cl}, \text{Br}, \text{and I}$). The photon energies labeled **a**, **b** and **c** were used as the excitation energies in the subsequent RIXS measurements.

II. METHOD

A. Experimental Method

We performed Cr L -edge ultra-high resolution RIXS measurements on CrX_3 at the 41A RIXS beamline of the Taiwan Photon Source (TPS) [22]. Figure 1(b) illustrates the scattering geometry of RIXS measurements. The crystalline c -axis was aligned within the horizontal scattering plane (π -polarization)

during the measurements. Cr L -edge XAS data was acquired prior to the RIXS measurements to determine the excitation photon energies. For the RIXS measurements, the tuned incident soft x-rays were directed at an angle (θ) of 90° to the sample surface (normal incidence), and the spectrometer was set at 140° (ω) back-scattering geometry with respect to the incoming photon beam. The instrumental energy resolution was ~ 30 meV.

Complementary XAS and RIXS measurements were performed at the PEAXIS beamline, BESSY II, Germany, with a resolution of 120 meV. CrX_3 single crystals were commercially obtained from HQ Graphene, and their crystallinity was verified using lab-based x-ray diffraction. Due to the samples' high hygroscopicity and sensitivity to oxygen, the CrX_3 samples were stored and handled under an inert gas atmosphere (Ar) in a glovebox environment to minimize air exposure. The samples were subjected to scotch tape exfoliation before being transferred to the experimental chamber to ensure a clean surface.

B. Computational Simulations

The quantum many-body script language QUANTY [23, 24] was used to simulate the experimental CrX_3 XAS and RIXS spectra. The Hamiltonian that describes the electronic structure of the system was built

using Multiplet ligand field theory (MLFT) [23, 25, 26]. The relevant electronic configurations in Cr^{3+} for the RIXS process consist of a ground state $2p^63d^3$ with an intermediate excited state $2p^53d^4$ followed by a de-excitation to the ground state. They resulted in atomic multiplets, which are described by $3d - 3d$ Coulomb and $2p - 3d$ exchange interactions parameterized in Slater-Condon integrals F_{dd}^k , F_{pd}^k (Coulomb), and G_{pd}^k (Exchange) for Hatree-Fock calculations [19, 23]. The Racah B and Racah C parameters were used to account for the ion covalency, which can be related to the F_{dd}^2 and F_{dd}^4 by Racah B = $(9F_{dd}^2 - 5F_{dd}^4)/441$ and Racah C = $5F_{dd}^4/63$ [27]. The ligand-to-metal charge transfer (LMCT) parameters were incorporated to consider the hopping between the halide ions and Cr^{3+} metal ions.

Local symmetry is a crucial parameter that can greatly influence the electronic, magnetic, and optical properties [28]. Although the perfect octahedral (O_h) symmetry has been commonly assumed for CrX_3 [8, 21, 29], some reports indicate a distorted O_h orientation in CrX_3 ; namely D_{3d} [30] and C_3 [31, 32] have been argued to give better explanations of some experimental findings. Notably, C_3 symmetry is a subgroup of the D_{3d} symmetry [33]. Since the ultra-high-resolution RIXS spectra enabled us to resolve multiple peak splittings, atomic mul-

tiplet RIXS spectra calculations using lower symmetry C_3 reproduced the experimental RIXS spectra more reliably.

III. RESULTS

A. XAS and RIXS

Figure 1(c) shows the Cr L -edge XAS spectra acquired from 570 to 600 eV at room temperature (RT) in total electron yield (TEY) mode. During the XAS process, the $2p^63d^3$ ground state electrons are excited to the $2p^53d^4$ state. Therefore, spectral features are dominated by dipole transitions from the core $2p$ level to the empty $3d$ states. Consequently, the two primary peaks observed in the XAS data can be attributed to the L_3 (~ 575 - 580 eV) and L_2 (~ 583 - 590 eV) lines [21, 34]. The L_3 -edge (**b** in Fig. 1(c)) shifts toward a lower energy as the halogen changes from Cl to Br to I. The energies **a**, **b**, and **c** were used as the excitation energies for the RIXS measurements.

Figure 2(a) shows the experimental RIXS spectra measured at RT. The main peak at 0 eV can be attributed to the elastic feature, where the incident photon beam energy E_{in} equals the scattered photon beam energy E_{out} . The nonzero spectral features are divided into three regions: I (~ 1 - 2 eV), II (~ 2 - 2.75 eV), and III (~ 2.75 - 4 eV). All RIXS

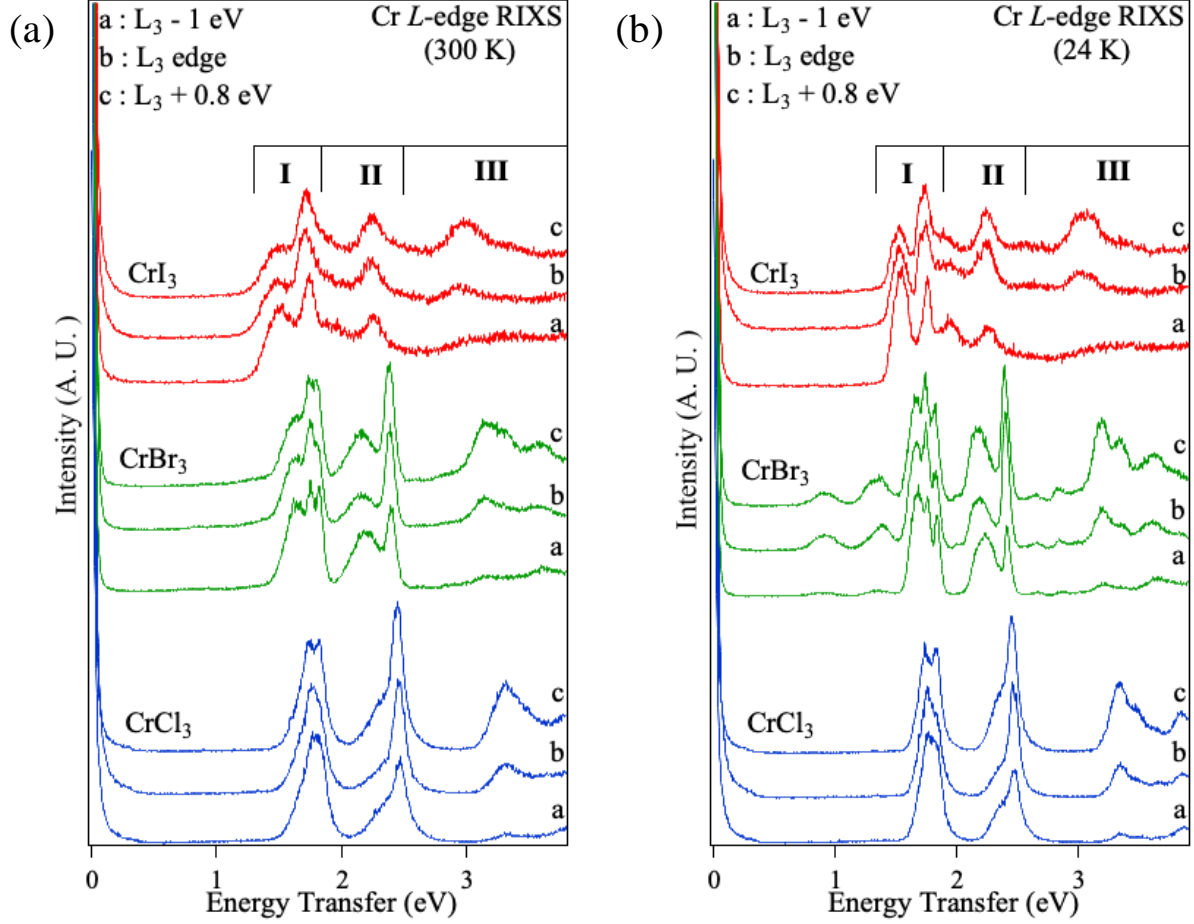


FIG. 2. (a) Cr L_3 -edge RIXS data measured in CrX_3 at 300 K and (b) at 24 K. The RIXS data have been collected at three different excitation energies: **a**, **b**, and **c** (see Figure 1(c)). The three regions, I, II, and III, show different spectral features in RIXS spectra. All spectra are normalized to the main peak in region I.

spectra were normalized to the main peak intensity in Region I to facilitate comparison. The three regions, I, II, and III, contain spectral features that can be attributed to the inter-orbital dd excitations. In this report, we only focus on d -site electronic structure and related excitations. Spectral features related to the CT process above 4 eV will be discussed elsewhere (see Appendix A).

The prominent peaks in region I exhibit maximum peak intensities at ~ 1.77 eV, 1.75 eV, and 1.72 eV for CrCl_3 , CrBr_3 , and CrI_3 , respectively. These energies downshift as the halogen changes from Cl to Br to I, consistent with the Cr L_3 XAS peak shift. In this region, CrCl_3 shows a single peak, while CrBr_3 shows a shoulder feature, and CrI_3 reveals a distinct splitting of the shoulder and the

main peak. This splitting becomes more pronounced from Cl to I. In region II, CrCl_3 shows a main peak with a shoulder characteristic, and CrBr_3 shows a clear separation between two peaks, while the shoulder characteristic in CrI_3 is dominated by the main peak in region I. Region III consists of more broadened multiple subpeaks in all three materials. The energy loss values in the aforementioned dd regions are independent of the incident energies and are known as Raman-like losses. However, the spectral intensities increase with the excitation energies (from **a** to **c** in Fig. 2). These resonant and Raman behaviors justify the attribution of these peaks to the well-known dd excitations.

Since CrX_3 shows structural and magnetic phase transitions at different temperatures, we repeated the RIXS measurements at low temperature (LT) of 24 K (see Fig. 2(b)). At 24 K, CrCl_3 is not magnetically ordered, while CrBr_3 and CrI_3 are magnetically ordered. The same energy regions are demarcated in the LT RIXS spectra, and the spectral features are much sharper. While the main peaks in regions I and II remain at the same energy transfer value in all CrX_3 at LT, the shoulder features gain more intensities and move closer to the main peak. For CrBr_3 , several extraneous peaks are observed in LT RIXS data from 0 to 1.5 eV. Neither BESSY II nor ALS [21] RIXS data show additional

spectral features at LT in the range of 0 - 1.5 eV (see Appendix A). Hence, an extensive analysis must be completed to confirm these LT RIXS features in the 0 - 1.5 eV range, and the origin of these features remains to be clarified.

B. Energy Level Diagrams and RIXS Simulations

1. Energy Level Diagrams

In this study, electronic ELDs are utilized to analyze the spectral features observed in the experimental RIXS data. The ELDs are calculated by diagonalizing the standard ligand and field multiplet Hamiltonian. The results provide the number of excited states in the system, including the spin-allowed and spin-forbidden states, which can be directly compared with the RIXS spectral features to determine the corresponding energy scales.

The ELDs have been labeled with multi-electronic atomic states in the $\text{Cr}^{3+}(d^3)$ system. In a perfect octahedral environment with O_h symmetry, the Cr five d orbitals are split into two energy levels t_{2g} and e_g (see Fig. 3(b)). This crystal field splitting results in the division of the $3d$ multielectronic atomic quartet states into manifolds: ${}^4F \rightarrow {}^4A_{2g}$, ${}^4T_{2g}$, and ${}^4T_{1g}(1)$, and ${}^4P \rightarrow {}^4T_{1g}(2)$ [21, 35]. When the symmetry is lowered to C_3 , the t_{2g}

orbitals are further divided into two states, as shown in Fig. 3(c). In this configuration, the atomic state ${}^4T_{2g}$ further splits into 4A_1 and 4E , while the ${}^4T_{1g}$ splits into 4A_2 and 4E states (see Appendix B) [31, 32]. The energies of the three states e , a_1 , and e^* , can be written using the crystal field parameter Dq , and distortion parameters $D\tau$, and $D\sigma$ as follows : [33].

$$E_{e_g}^e = 6Dq + (7/3)D\tau \quad (1a)$$

$$E_{t_{2g}}^{a_1} = -4Dq - 2D\sigma - 6D\tau \quad (1b)$$

$$E_{t_{2g}}^{e^*} = -4Dq + D\sigma + (2/3)D\tau \quad (1c)$$

The initial parameters in the ELD calculations corresponding to the symmetry O_h were taken from the literature, as no values for the symmetry C_3 were reported. The Coulomb interaction U of 3.5 eV was used following Feldkemper *et. al* [36]. The ELD does not depend on the Coulomb interaction U , and its effect on the RIXS spectra is very small. The ratio between U_{dd} and U_{pd} was kept constant at 1.5 following Y. Shao *et. al.* [21]. The crystal field distortion parameters $D\tau$ and $D\sigma$ were determined to be 0.035 eV and -0.11 eV for CrCl_3 (see Appendix B). Figure 4(a) shows the ELD calculated as a function of the crystal field Dq in CrCl_3 . Dashed blue and solid red lines indicate the spin-doublet and spin-quartet states, respectively. The follow-

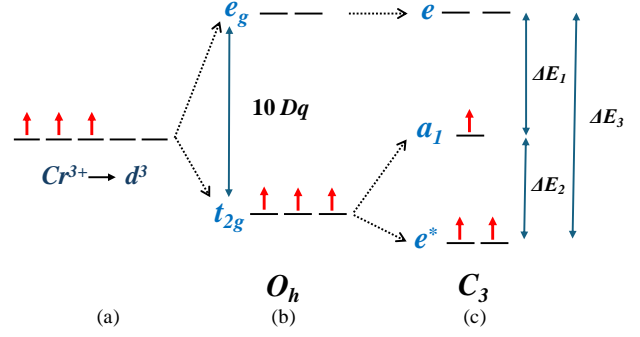


FIG. 3. (a) valence d orbital electron distribution in Cr^{3+} metal ion. (b) Lifting of degeneracy of the d^{3+} spectroscopic term (free F^{4+} ion) due to O_h symmetry. This configuration's 5 d orbitals are divided into two energy levels t_{2g} and e_g . (c) Lifting of the degeneracy of the d^{3+} electrons due to C_3 symmetry. The five d orbitals are divided into one a_1 state and two e states within the C_3 symmetry.

ing factors contribute to the determination of the crystal field Dq . In the O_h environment, the crystal field splitting $10Dq$ can be determined by considering the transition from the ${}^4A_{2g} \rightarrow {}^4T_{2g}$ states, which is equivalent to the energy transfer value of the maximum of the first spin-allowed band in experimental RIXS spectra [37]. Since the atomic state ${}^4T_{2g}$ splits into 4A_1 and 4E states within the C_3 symmetry configuration and the transition ${}^4A_2 \rightarrow {}^4A_1$ is dipole-forbidden, the maximum of the peak in region I (see Fig. 2(a)) can be assigned to the ${}^4A_2 \rightarrow {}^4E$ transition because the dipole-allowed quartet states will

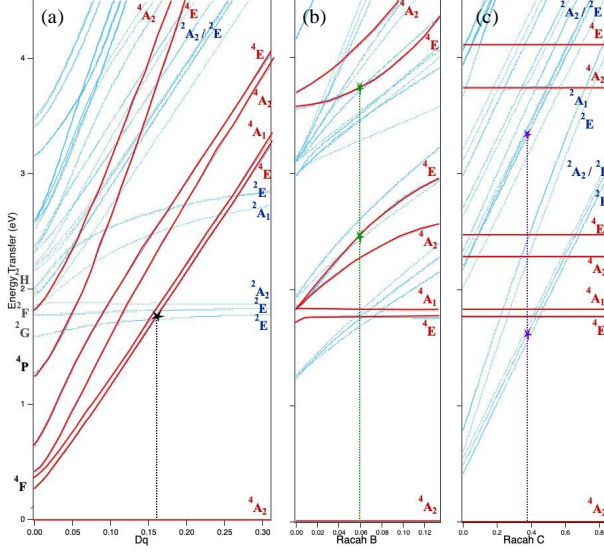


FIG. 4. (a) Tanabe-Sugano-like energy level diagrams as a function of crystal field Dq (b) Racah B and (c) Racah C in CrCl_3 . The quartet and doublet states in Cr^{+3} metal are shown by solid red and dashed blue lines, respectively. The black, green, and purple stars indicate the extracted Dq , Racah B and Racah C values by comparing the ELDs with experimental RIXS spectra shown in Fig. 2.

have a stronger intensity. Therefore, the crystal field splitting $10Dq$ can be determined to be 1.615 eV in CrCl_3 . The $10Dq$ values of CrBr_3 and CrI_3 were determined to be 1.48 eV and 1.21 eV, respectively, following the same process.

The Racah B was varied next, and the result is presented in Fig. 4(b). The two peaks in region II were assigned to 4A_2 and 4E . Their expected order of states and the energy gap were dependent on the crystal field

distortion parameter $D\tau$, which was determined to be -0.11 eV to match the experimental data (see Appendix B). The electronic transition $^4A_2 \rightarrow ^4E$ ($^4T_{1g}$) was considered in determining the Racah B values of 0.06 eV, 0.05 eV, and 0.04 eV in CrCl_3 , CrBr_3 and CrI_3 , respectively.

After tuning the $10Dq$ and Racah B values, the ELD was calculated as a function of Racah C, as shown in Fig. 4(c). At this stage, the quartet lines appear to be horizontal. However, the ELDs include several doublet states influenced by Racah B and Racah C. These doublet states represent the spin-flip electronic transitions. The SOC in the Cr $2p$ level can accompany the spin-flip electronic transition during the RIXS process, producing spin-forbidden doublet states with $S = 1/2$, as discussed in the latter. Racah C of 0.38 eV in all CrX_3 was determined after considering the transitions $^4A_2 \rightarrow ^2A_2$ and $^4A_2 \rightarrow ^2E$. A summary of the energy scales calculated in CrX_3 at both RT and LT are listed in Table I.

2. XAS/RIXS spectrum calculation

The XAS experimental data was used to tune the RIXS intermediate parameters as the RIXS process consists of an XAS process followed by a resonant X-ray emission (see Appendix C). The Slater integral pa-

TABLE I. Summary of the energy scales calculated for CrX_3 using MLFT calculations

	T	$10Dq$	$D\tau$	$D\sigma$	Racah B	Racah C	C/B
		(eV)	(eV)	(eV)	(eV)	(eV)	
CrCl_3	300 K	1.615	0.035	-0.110	0.060	0.380	6.333
CrBr_3	300 K	1.480	0.055	-0.140	0.050	0.380	7.600
CrI_3	300 K	1.210	0.090	-0.180	0.040	0.380	9.500
CrCl_3	24 K	1.625	0.032	-0.115	0.061	0.390	6.390
CrBr_3	24 K	1.510	0.050	-0.145	0.053	0.390	7.360
CrI_3	24 K	1.220	0.090	-0.185	0.038	0.390	10.260

rameters F_{pd}^2 , G_{pd}^1 , and G_{pd}^3 , which account for the electron exchange interactions $2p3d$, were tuned to match the experimental XAS data. Furthermore, the $2p_{3/2}$ and $2p_{1/2}$ spectral parts are clearly separated by the core-hole SOC and the core-hole lifetime broadening, which gives the sharp features [38]. The energy separation of 8.5 eV between the L_3 and L_2 peaks (Fig. 1(c)) suggested a Cr $2p$ SOC value of ~ 5.7 eV. Subsequently, we calculated the RIXS spectra using all refined parameters and compared them with the experimental RIXS data, as illustrated in Fig. 5. Panels (a), (c), and (e) show the RT simulations, while (b), (d), and (f) contain LT data. We only reported the experimental (solid black line) and simulated (dashed black line) RIXS spectra measured at the L_3 -edge (excitation energy **b**). Similar results were obtained for all the excitation energies.

The simulated RIXS spectra for each material show the fine spectral features and energy positions that are responsible for the main intensities in the experimental data. The peak positions extracted from the simulated RIXS spectra are shown below the RIXS spectra with red lines indicating spin-allowed quartet states and blue lines with spin-flip doublet states.

A clear energy gap between the spin-allowed quartets and spin-forbidden doublets in region I was observed for the first time with high resolution in RIXS data. This energy difference becomes more prominent as the halogen changes from Cl to Br to I, which justifies the well-separated shoulder features in the experimental RIXS data (see Fig. 5). The positions of the doublet states downshift as the halogen changes from Cr to I, showing a similar trend to the quartet states. Two

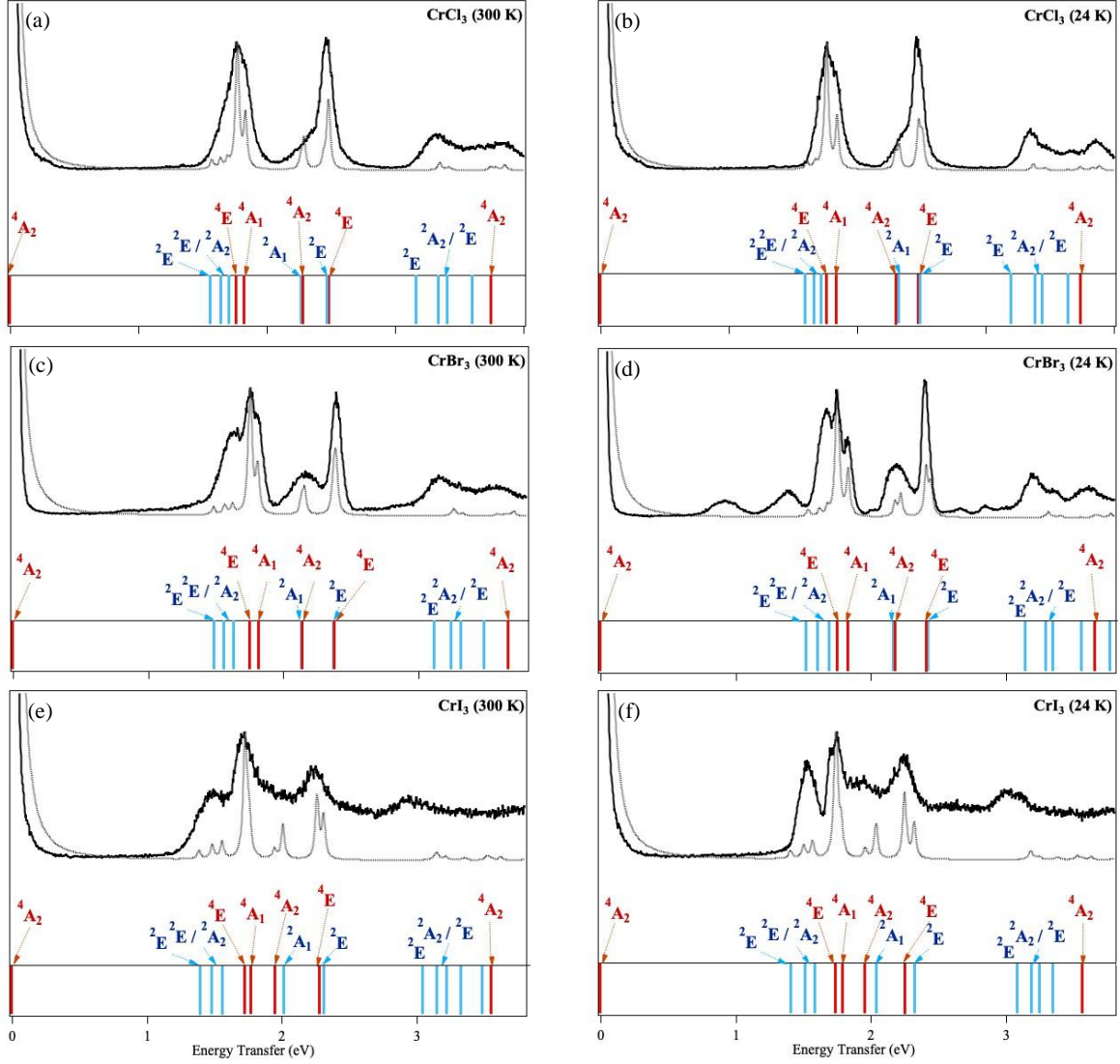


FIG. 5. LT and RT RIXS simulations at Cr L_3 edge in (a)-(b) CrCl_3 (c)-(d) CrBr_3 , and (e)-(f) CrI_3 . Experimental(simulated) data are shown in the black solid(dashed) line. Spin multiplicity analysis of CrX_3 $3d-3d$ states are shown below the RIXS spectra with Red and blue bands indicating the spin-quartets and spin-doublets states. These states are identified through the ELD calculations shown in Fig. 4.

peaks observed in region II primarily depend on the crystal field distortion parameter $D\tau$, and they are attributed to 4A_1 and 4E , justifying the distorted octahedral orientation with C_3 symmetry in CrX_3 . The separa-

tion between the doublet and quartet states in this region decreases drastically. There is a slight mismatch between the experimental RIXS data and the simulated RIXS spectra in region III due to the cluster of doublets

(see Fig. 4) and CT excitations, which we haven't discussed in this study.

As the temperature is lowered to 24 K, the shoulder features shift closer to the main peaks. The shoulder features in region I consist of spin-forbidden doublet states 2E and 2A_1 . As the temperature decreases, the spins begin to align in an ordered arrangement, causing the spin-forbidden electronic excitations to acquire higher energies, which results in a shift of the peaks at LT. In region II, the separation of the two peaks primarily depends on the crystal field distortion parameters $D\tau$. Since CrX_3 exhibits both MPT and SPT at different temperatures, the SPT can cause a change in octahedral distortion, resulting in different crystal field distortion parameters and, consequently, different electronic structure parameters.

The schematic representation of Cr $2p3d$ RIXS in Figure 6 (a),(b) shows the electronic excitations from the initial ground state through the intermediate core-excited to the final valence-excited states. Figure 6 (a) shows the electronic excitation corresponding to the spin-allowed quartet states, where the total spin moment of the ground state and the final state is $S = 3/2$ ($2S + 1 = 4$), indicating a conserved spin moment during the RIXS process. On the other hand, Figure 6 (b) shows the electronic excitation that corresponds to the spin-forbidden (spin-

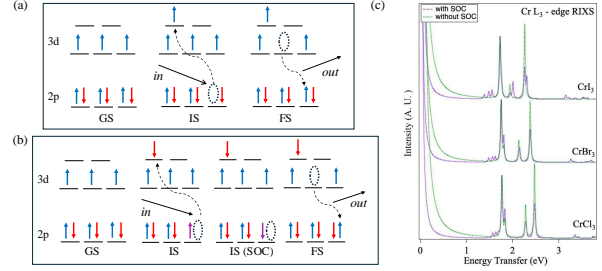


FIG. 6. (a) Electronic excitation corresponds to the spin-allowed quartet state. The ground state (GS), intermediate state (IS), and final state (FS) electron configurations are indicated. The spin moment is conserved throughout the process. (b) Electronic excitation for the spin-flip doublet state. The incident and scattered x-rays are labeled as *in* and *out*, respectively. (c) RIXS spectra comparison with the contribution of SOC (purple) and without SOC (green) in Cr metal ion.

flip) doublet states, where the total spin moment changes from $S = 3/2$ to $S = 1/2$ ($2S + 1 = 2$) from the ground state to the final state, indicating a spin-flip during the process. The presence of Cr $2p$ spin-orbit interaction, given by the Cr $2p$ spin-orbit parameter $\zeta(2p)$ (5.668 eV), which is much stronger than the $3d$ spin-orbit interactions, given by the Cr $3d$ spin-orbit parameter $\zeta(3d)$ (0.018 eV), contributes to this spin-flip and enables spin-forbidden states to gain intensity [38, 39]. The simulated RIXS spectra effectively capture this effect, as shown in Fig. 6 (c), in agreement with the experimental ob-

servations. We have identified two single electron excitations; $t_{2g}^3 \rightarrow t_{2g}^2 e_g^1$ corresponds to the ${}^4A_{2g} \rightarrow {}^4T_{2g}$ and ${}^4A_{2g} \rightarrow {}^4T_{1g}$ multiplet transitions, and one double electron excitation $t_{2g}^3 \rightarrow t_{2g}^1 e_g^2$ corresponds to the ${}^4A_{2g} \rightarrow {}^4T_{1g}$ multiplet transition in the O_h symmetry [30].

IV. DISCUSSION

We have collected ultra-high resolution RIXS spectra for CrX_3 and presented a detailed electronic structure parameter calculation, including the determination of the crystal field splitting and Racah parameters in CrX_3 . Now, we discuss how the obtained values relate to previously determined electronic structure parameters in CrX_3 . The extracted energies of the spin-quartet and spin-doublet states are consistent with the d^3 ELDs in Cr^{3+} systems [19, 21]. Density functional theory calculations predict that the magnetic moment is hosted predominantly in the Cr^{3+} ions with an $S = 3/2$ spin configuration and a reported spin moment of $3\mu_B/\text{Cr}$ [40–42]. From our calculations, the spin moment of the Cr was determined to be $3.7497 \mu_B/\text{Cr}$, indicating a larger value compared to the nominal spin moment in Cr due to the ligand contribution [21, 43].

Shao *et.al.* reported $10Dq$ values of 1.55 eV, 1.45 eV, and 1.45 eV for CrCl_3 , CrBr_3 ,

TABLE II. Crystal field splitting in CrX_3 . All values are in eV.

	CrCl_3 (300K)	CrCl_3 (24K)	CrBr_3 (300K)	CrBr_3 (24K)	CrI_3 (300K)	CrI_3 (24K)
$E_{e_g}^e$	1.05	1.05	1.02	1.02	0.94	0.94
$E_{t_{2g}}^{a_1}$	-0.64	-0.62	-0.64	-0.61	-0.66	-0.66
$E_{t_{2g}}^{e*}$	-0.73	-0.74	-0.70	-0.72	-0.60	-0.61
ΔE_1	1.69	1.67	1.66	1.64	1.60	1.60
ΔE_2	0.10	0.13	0.05	0.10	-0.06	-0.05
ΔE_3	1.78	1.80	1.71	1.74	1.54	1.56

and CrI_3 , respectively, assuming O_h symmetry [21] in the metal Cr ion. With the improved energy resolution of our RIXS measurements, we could refine the $10Dq$ parameter using C_3 symmetry with distorted octahedral orientation in CrX_3 . This highlights the need for high-resolution RIXS measurements to determine the electronic structure parameters precisely. The trend of decrease in the refined $10Dq$ values from our study (1.615 eV, 1.480 eV, and 1.210 eV for CrCl_3 , CrBr_3 , and CrI_3 respectively) is more clear as the halogen changes from Cl to Br to I. This is in good agreement with the spectrochemical series explaining the strength of various ligand-induced crystal fields: $\text{I}^{-1} < \text{Br}^{-1} < \text{Cl}^{-1}$ [44]. As the temperature lowers to 24 K, the $10Dq$ increases in CrX_3 , which indicates a substantial exchange splitting of the states. This may be due to the FM Cr-I-

TABLE III. Summary of the electronic structure parameters calculated for CrX_3 . All values are in eV.

	CrCl_3	CrBr_3	CrI_3
$F_{dd}^2(3d^3)$	5.600 (52.0%)	5.110 (47.4%)	4.620 (42.9%)
$F_{dd}^4(3d^3)$	4.788 (70.9%)	4.788 (70.9%)	4.788 (70.9%)
$F_{dd}^2(2p^5 3d^4)$	6.025 (52.0%)	5.500 (47.4%)	4.971 (42.9%)
$F_{dd}^4(2p^5 3d^4)$	5.154 (70.9%)	5.154 (70.9%)	5.154 (70.9%)
$F_{pd}^2(2p^5 3d^4)$	5.873 (90%)	5.546 (85%)	4.894 (75%)
$G_{pd}^1(2p^5 3d^4)$	3.015 (63%)	2.871 (60%)	2.632 (55%)
$G_{pd}^3(2p^5 3d^4)$	1.769 (65%)	1.769 (65%)	1.769 (65%)
$\text{SOC}_{3d}(3d^3)$	0.018 (50%)	0.018 (50%)	0.018 (50%)
$\text{SOC}_{3d}(2p^5 3d^4)$	0.018 (50%)	0.018 (50%)	0.018 (50%)
$\text{SOC}_{2p}(2p^5 3d^4)$	5.668 (100%)	5.668 (100%)	5.668 (100%)
Δ	3.800	3.300	3.000
$10DqL$	0.103	0.238	0.032
$V_e(e_g)$	1.992	1.940	1.836
$V_{a1}(t_{2g})$	1.320	1.380	1.400
$V_{e*}(t_{2g})$	1.320	1.380	1.400

Cr superexchange interaction in CrX_3 across different temperatures [45].

The determined crystal field distortion parameters (see Table I) show opposite signs: negative for $D\sigma$ and positive for $D\tau$. This indicates an opposite sign relation with the crystal field distortion parameters in ruby, justifying the sign of optical anisotropy in CrX_3 [19, 32]. The energies of each Cr d orbital in CrX_3 were calculated using equation 1 as summarized in Table II. The energies of each orbital imply that the e^* and a_1 states

are in the conduction band, while the e state is in the valence band. The e^* and a_1 states are switched in CrI_3 . The energy gap between each state is given by ΔE_1 , ΔE_2 , and ΔE_3 (see Fig. 3). It is shown that the ΔE_1 and ΔE_3 decrease as the halogen changes from Cl to I while ΔE_2 increases, indicating the possibility of having a low-spin state as the halogen changes to I.

A summary of the electronic structure parameters used in the RIXS simulations are listed in the Table III, including the LMCT

parameters. Note that the unequal scaling in Hatree-Fock Slater integrals F_{dd}^2 and F_{dd}^4 , and the exchange parameters G_{pd}^1 and G_{pd}^3 is essential to reproduce the RIXS spectra. The Racah B parameter, which accounts for inter-electronic repulsion, shows a decreasing trend as the halogen changes from Cl to Br to I, agreeing with the nephelauxetic effect. These values reflect the increasing covalency that is observed from $\text{Cl} < \text{Br} < \text{I}$ with higher scaling of the Hatree-Fock parameters corresponding to the ionic interactions and lower scaling corresponding to the covalent interactions [21, 25, 30, 44]. The Racah C values do not change as the halogen varies. The Racah A was ignored because it is considered the same for any metal ion. The determined C/B ratios at RT of 6.333, 7.6, and 9.5 were higher than the literature-reported values. The Racah B parameter primarily determines the ratio C/B as the Racah C is constant. It increases with the halogen change from Cl to I, reflecting the shift from ionic bonding in CrCl_3 to covalent bonding in CrI_3 .

The SOC in CrX_3 plays a significant role in the spin-flip (spin-forbidden) process, as discussed earlier. Recent studies suggest that the spin-flip excitations are responsible for the anisotropic SOC, which, in turn, contributes to the Dzyaloshinskii-Moriya (DM) interaction [8, 46]. However, further investigations are needed to better understand the

relationship between the strength of SOC and its influence on DM interaction. This study lays an important foundation for future investigations into CrX_3 as a material for spintronic and optoelectronic devices, where precise control over electronic and optical properties is crucial for achieving advanced functionalities.

V. CONCLUSIONS

We conducted Cr $2p - 3d$ XAS and Cr L -edge ultra-high resolution RIXS measurements on CrX_3 . Atomic multiplet RIXS simulations, interpreted using the MLFT approach, showed good agreement with the experimental RIXS data, as illustrated in Fig. 5. This study marks the first experimental observation of clear energy separations between spin-allowed and spin-forbidden electronic transitions in CrX_3 using the improved high-resolution RIXS measurements. By applying ELDs in atomic multiplet calculations, we have refined the electronic energy scales, taking into account the distorted octahedral orientation with C_3 symmetry in CrX_3 , as detailed in Table I. These findings indicate that the ligand substitution significantly affects the d -orbital electronic structure. The superexchange coupling effect on the inter-atomic orbital splitting was discussed, as well as the DM interactions and the role of SOC in

the spin-forbidden excitations. We propose that investigating RIXS on few-layer CrX_3 samples could offer deep insights into the electronic structure properties of these materials. Further investigations are needed to understand the low-energy RIXS spectral features in the 0 - 1.5 eV range.

ACKNOWLEDGMENTS

This research was conducted at 41A RIXS beamline, Taiwan Photon Source (TPS), and PEAXIS RIXS beamline, BESSY II, Germany operated by the Helmholtz-Zentrum Berlin für Materialien und Energie. The preliminary RIXS measurements were taken at the qRIXS 8.0.1 beamline, Advanced Light Source (ALS), which is a DOE Office of Science User Facility under contract no. DE-AC02-05CH11231. We thank all the beamline scientists for their valuable support. Y.C.S. acknowledges the financial support from the National Science and Technology Council (NSTC) in Taiwan under grant nos. 113-2112-M-213-025-MY3. The Welch Foundation (grant number: E-0001) and the Texas Center for Superconductivity (TCSUH) supported work at the University of Houston. Part of this work was supported by the U.S. DOE, BES, under Award No. DE-SC0024332. The authors acknowledge support from the U.S. Air Force Office of

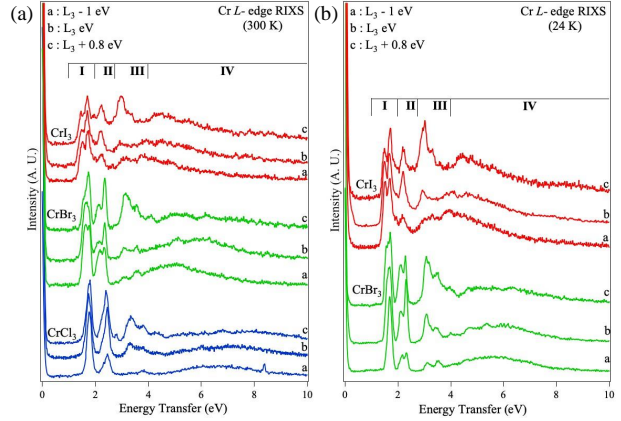


FIG. 7. (a) Cr L_3 -edge RIXS data measured in CrX_3 at 300 K and (b) at 13 K. The incident photon beam was normal to the sample surface, and the spectrometer was at 140° . The RIXS data have been collected at three excitation energies: **a**, **b**, and **c**.

Scientific Research and Clarkson Aerospace Corp. under Award FA9550-21-1-0460. Special thanks to the eXn group members at the University of Houston.

Appendix A: Comparison of RIXS experimental data from different beamlines

We have performed complementary XAS and RIXS measurements at the PEAXIS beamline, BESSY II, Germany, with an energy resolution of ~ 120 meV [47]. Figure 7 shows the RIXS data collected at Cr L -edge in RT and LT in the energy transfer scale of 0 - 10 eV where I, II, and III can be attributed to inter-orbital dd excitations and region IV as dipole-allowed LMCT excita-

tions (see main text). The RIXS measurements were taken at three excitation energies, **a**, **b**, and **c**, similar to the main text. While RIXS data were measured for all three materials at RT, the LT RIXS data were only measured for CrBr₃ and CrI₃. The improved resolution has resulted in sharpening of spectral features justifying the need of high resolution RIXS data for better determination of electronic structure parameters as explained in main text. No significant spectral feature differences exist between RT and LT RIXS data in the 0 - 1.5 eV range. However, Figure 2(b) in the main text shows extraneous peaks that were not observed in the RT RIXS spectra. Given the discrepancies across different beamlines, more study is needed to determine the nature of these extraneous features.

Moreover, several published reports have focused on this energy region. Reports indicate a sign opposition in coupling between exciton and magnetization in CrBr₃ and CrI₃ that may result in different amplitudes in RIXS spectra through optical spin pumping experiments [48]. This agrees with our RIXS data in the main text, where CrBr₃ shows higher intensities in the spectral features in the 0 - 1.5 eV range than CrCl₃ and CrI₃. On the other hand, exciton peaks have been reported in CrX₃ predicting a peak 1 eV [49]. Regardless, it is still debatable whether the spectral features in the 0 - 1.5 eV range can

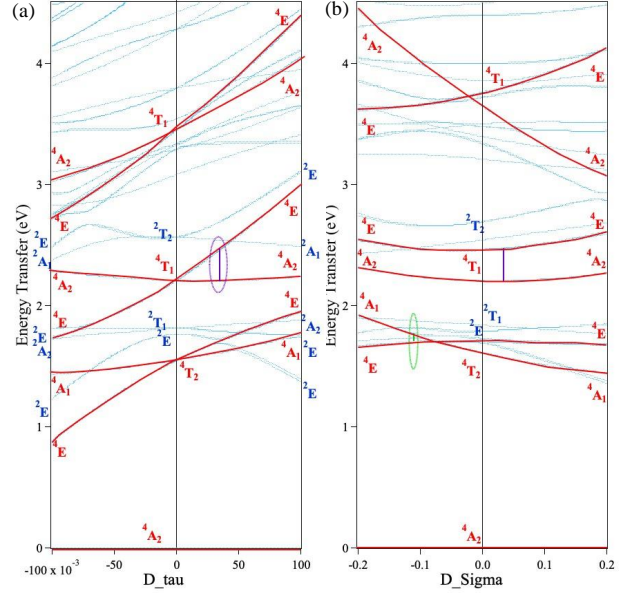


FIG. 8. a) Energy-level diagram by varying the C_3 crystal field distortion parameter $D\tau$ and b) $D\sigma$. At $D\sigma = D\tau = 0$ eV, spectroscopic terms are labeled in O_h symmetry, else they are labeled in C_3 symmetry. The red and blue lines indicate the quartet and doublet states, respectively.

be understood.

Appendix B: Determination of crystal field distortion parameters CrCl₃

The determination of crystal field distortion parameters was carried out under several stages. The multielectronic eigenstates in d^{+3} system were identified for the O_h and C_3 symmetries. First, the ELD was calculated by varying $D\tau$ for CrCl₃ as shown in Figure 8(a). Notice the atomic states $4T_{2g}$ further splits into $4A_1$ and $4E$, while $4T_{1g}$ state

splits into 4A_2 and 4E when the symmetry is changed from O_h to C_3 . de Groot reported a ~ 100 meV splitting between 4A_2 and 4E for ruby. On the contrary, Pollini *et.al.* reported a splitting of ~ 88 meV for CrCl_3 with the opposite sign for optical anisotropy compared to ruby [19, 50]. However, the preliminary peak fitting in the studied experimental RIXS data resulted in an energy gap of ~ 0.28 eV between the peaks 4A_2 and 4E . This resulted in $D\tau$ being 0.035 eV for CrCl_3 with the order of ${}^4E > {}^4A_2$ to match the experimental RIXS data and agree with the reported values. (see Figure 8(a)) [32].

Keeping $D\tau$ at the selected value, $D\sigma$ was changed, and the ELD was calculated as shown in 8(b). The same procedure was followed to determine $D\sigma$ and, $D\sigma = -0.11$ eV matched the expected peak splitting with ${}^4A_1 > {}^4E$ in the experimental RIXS data [32].

Appendix C: XAS simulation for CrX_3 (X= Cl, Br, and I)

Figure 9 compares the experimental XAS spectra with the calculated XAS spectra for CrX_3 . The initial parameters for the calculation were obtained from the main text. The electron exchange interactions in the excited state were addressed using the Slater parameters G_{pd}^1 and G_{pd}^3 . The excited state parameters were tuned to match the experimental

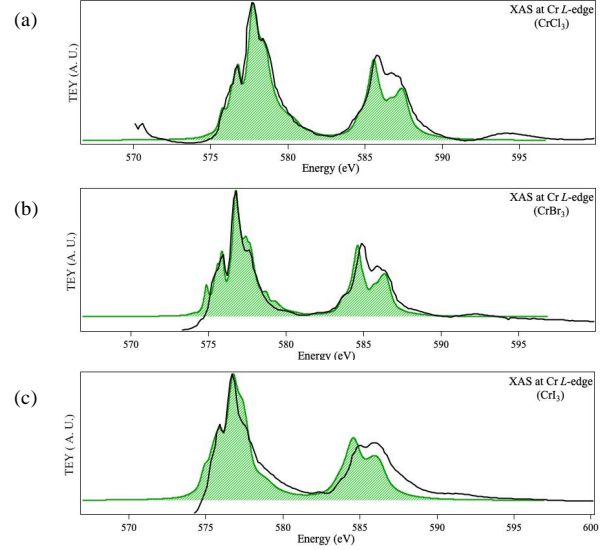


FIG. 9. XAS Experimental data compared with Quanty simulated XAS spectra for a) CrCl_3 , a) CrBr_3 , and a) CrI_3 . The black lines show the experimental XAS data, and the green shaded area shows the Quanty simulated XAS spectra. XAS data. Similar scaling of the Slater integrals resulted in a mismatch with experimental data. The spectral shape was significantly improved with unequal scaling of F_{dd}^2 and F_{dd}^4 parameters, but G_{pd}^1 and G_{pd}^3 also resulted in additional improvements.

BIBLIOGRAPHY

- [1] Suchanda Mondal, A Midya, Manju Mishra Patidar, V Ganesan, and Prabhat Mandal. Magnetic and magnetocaloric properties of layered van der Waals CrCl_3 . *Applied Physics Letters*, 117(9), 2020.

- [2] Ichiro Tsubokawa. On the magnetic properties of a CrBr_3 single crystal. *Journal of the Physical Society of Japan*, 15(9):1664–1668, 1960.
- [3] Bevin Huang, Genevieve Clark, Efrén Navarro-Moratalla, Dahlia R Klein, Ran Cheng, Kyle L Seyler, Ding Zhong, Emma Schmidgall, Michael A McGuire, David H Cobden, et al. Layer-dependent ferromagnetism in a van der waals crystal down to the monolayer limit. *Nature*, 546(7657):270–273, 2017.
- [4] Jan CA Boeyens. The periodic electronegativity table. *Zeitschrift für Naturforschung B*, 63(2):199–209, 2008.
- [5] L Craco, SS Carara, Y-C Shao, Y-D Chuang, and B Freelon. Electronic structure of rhombohedral CrX_3 ($\text{X} = \text{Br}, \text{Cl}, \text{I}$) van der waals crystals. *Physical Review B*, 103(23):235119, 2021.
- [6] John B Goodenough. *Magnetism and the chemical bond*. R. E. Krieger Pub. Co., 1963.
- [7] N David Mermin and Herbert Wagner. Absence of ferromagnetism or antiferromagnetism in one-or two-dimensional isotropic heisenberg models. *Physical Review Letters*, 17(22):1133, 1966.
- [8] Anirudha Ghosh, H Johan M Jönsson, Deepak John Mukkattukavil, Yaroslav Kvashnin, Dibya Phuyal, Patrik Thunström, Marcus Agåker, Alessandro Nicolaou, Martin Jonak, Rüdiger Klingeler, et al. Magnetic circular dichroism in the dd excitation in the van der waals magnet CrI_3 probed by resonant inelastic x-ray scattering. *Physical Review B*, 107(11):115148, 2023.
- [9] Shengwei Jiang, Lizhong Li, Zefang Wang, Kin Fai Mak, and Jie Shan. Controlling magnetism in 2d CrI_3 by electrostatic doping. *Nature nanotechnology*, 13(7):549–553, 2018.
- [10] K S Novoselov, Artem Mishchenko, Alexandra Carvalho, and AH Castro Neto. 2d materials and van der waals heterostructures. *Science*, 353(6298):aac9439, 2016.
- [11] Longfei Pan, Le Huang, Mianzeng Zhong, Xiang-Wei Jiang, Hui-Xiong Deng, Jingbo Li, Jian-Bai Xia, and Zhongming Wei. Large tunneling magnetoresistance in magnetic tunneling junctions based on two-dimensional CrX_3 ($\text{X} = \text{Br}, \text{I}$) monolayers. *Nanoscale*, 10(47):22196–22202, 2018.
- [12] Muhammad Akram, Harrison LaBollita, Dibyendu Dey, Jesse Kapeghian, Onur Erten, and Antia S Botana. Moiré skyrmions and chiral magnetic phases in twisted CrX_3 ($\text{X} = \text{I}, \text{Br}, \text{and Cl}$) bilayers. *Nano Letters*, 21(15):6633–6639, 2021.
- [13] SR Singamaneni, LM Martinez, J Niklas, OG Poluektov, R Yadav, M Pizzochero,

- OV Yazyev, and MA McGuire. Light induced electron spin resonance properties of van der waals crx_3 ($x = \text{cl}, \text{i}$) crystals. *Applied Physics Letters*, 117(8), 2020.
- [14] Prakash Mishra and Tunna Baruah. Magnetic properties of crx_3 ($x = \text{cl}, \text{br}, \text{i}$) monolayers in excited states. *Journal of Materials Chemistry C*, 12:5216–5221, 2024.
- [15] Azkar Saeed Ahmad, Yongcheng Liang, Mingdong Dong, Xuefeng Zhou, Leiming Fang, Yuanhua Xia, Jianhong Dai, Xiaozhi Yan, Xiaohui Yu, Junfeng Dai, et al. Pressure-driven switching of magnetism in layered crcl_3 . *Nanoscale*, 12(45):22935–22944, 2020.
- [16] Satoru Sugano. *Multiplets of Transition-Metal Ions in Crystals*. Elsevier, 1970.
- [17] MI Katsnelson and AI Lichtenstein. Theory of optically forbidden d–d transitions in strongly correlated crystals. *Journal of Physics: Condensed Matter*, 22(38):382201, 2010.
- [18] Benjamin E Van Kuiken, Anselm W Hahn, Dimitrios Maganas, and Serena DeBeer. Measuring spin-allowed and spin-forbidden d–d excitations in vanadium complexes with 2p3d resonant inelastic x-ray scattering. *Inorganic Chemistry*, 55(21):11497–11501, 2016.
- [19] Myrtille OJY Hunault, Yoshihisa Harada, Jun Miyawaki, Jian Wang, Andries Meijerink, Frank MF De Groot, and Matti M Van Schooneveld. Direct observation of cr^{3+} 3d states in ruby: Toward experimental mechanistic evidence of metal chemistry. *The Journal of Physical Chemistry A*, 122(18):4399–4413, 2018.
- [20] Luuk JP Ament, Michel Van Veenendaal, Thomas P Devereaux, John P Hill, and Jeroen Van Den Brink. Resonant inelastic x-ray scattering studies of elementary excitations. *Reviews of Modern Physics*, 83(2):705, 2011.
- [21] YC Shao, B Karki, W Huang, X Feng, G Sumanasekera, J-H Guo, Y-D Chuang, and B Freelon. Spectroscopic determination of key energy scales for the base hamiltonian of chromium trihalides. *The journal of physical chemistry letters*, 12(1):724–731, 2021.
- [22] A. Singh, H. Y. Huang, Y. Y. Chu, C. Y. Hua, S. W. Lin, H. S. Fung, H. W. Shiu, J. Chang, J. H. Li, J. Okamoto, C. C. Chiu, C. H. Chang, W. B. Wu, S. Y. Perng, S. C. Chung, K. Y. Kao, S. C. Yeh, H. Y. Chao, J. H. Chen, D. J. Huang, and C. T. Chen. Development of the Soft X-ray AGM–AGS RIXS beamline at the Taiwan Photon Source. *Journal of Synchrotron Radiation*, 28(3):977–986, May 2021.
- [23] Maurits W Haverkort. Quanta for core level spectroscopy-excitons, resonances and band

- excitations in time and frequency domain. In *Journal of Physics: Conference Series*, volume 712, page 012001. IOP Publishing, 2016.
- [24] Marius Retegan and Stephan Kuschel. mretegan/crispy: v0.7.4, 2023.
- [25] MW Haverkort, M Zwierzycki, and OK Andersen. Multiplet ligand-field theory using wannier orbitals. *Physical Review B*, 85(16):165113, 2012.
- [26] Frank De Groot and Akio Kotani. *Core level spectroscopy of solids*. CRC press, 2008.
- [27] Giulio Racah. Theory of complex spectra. i. *Physical Review*, 61(3-4):186, 1942.
- [28] Myrtille OJY Hunault, Laurence Galois, Gérald Lelong, Matt Newville, and Georges Calas. Effect of cation field strength on Co^{2+} speciation in alkali-borate glasses. *Journal of Non-Crystalline Solids*, 451:101–110, 2016.
- [29] Kyle L Seyler, Ding Zhong, Dahlia R Klein, Shiyuan Gao, Xiaou Zhang, Bevin Huang, Efrén Navarro-Moratalla, Li Yang, David H Cobden, Michael A McGuire, et al. Ligand-field helical luminescence in a 2d ferromagnetic insulator. *Nature Physics*, 14(3):277–281, 2018.
- [30] Mihail Atanasov, Dmitry Ganyushin, Kantharuban Sivalingam, and Frank Neese. A modern first-principles view on ligand field theory through the eyes of correlated multireference wavefunctions. *Molecular electronic structures of transition metal complexes II*, pages 149–220, 2012.
- [31] J.F. Dillon, H. Kamimura, and J.P. Remika. Magneto-optical properties of ferromagnetic chromium trihalides. *Journal of Physics and Chemistry of Solids*, 27(9):1531–1549, 1966.
- [32] I Pollini and G Spinolo. Intrinsic optical properties of CrCl_3 . *Physica status solidi (b)*, 41(2):691–701, 1970.
- [33] Amélie Juhin, Christian Brouder, Marie-Anne Arrio, Delphine Cabaret, Philippe Saintavrit, Etienne Balan, Amélie Bordage, Ari P Seitsonen, Georges Calas, Sigrid G Eeckhout, et al. X-ray linear dichroism in cubic compounds: The case of Cr^{3+} in MgAl_2O_4 . *Physical Review B*, 78(19):195103, 2008.
- [34] Michele Serri, Giuseppe Cucinotta, Lorenzo Poggini, Giulia Serrano, Philippe Saintavrit, Judyta Strychalska-Nowak, Antonio Politano, Francesco Bonaccorso, Andrea Caneschi, Robert J Cava, et al. Enhancement of the magnetic coupling in exfoliated CrCl_3 crystals observed by low-temperature magnetic force microscopy and x-ray magnetic circular dichroism. *Advanced Materials*, 32(24):2000566, 2020.

- [35] Vincent Vercamer, Myrtille OJY Hunault, Gérald Lelong, Maurits W Haverkort, Georges Calas, Yusuke Arai, Hiroyuki Hijiya, Lorenzo Paulatto, Christian Brouder, Marie-Anne Arrio, et al. Calculation of optical and k pre-edge absorption spectra for ferrous iron of distorted sites in oxide crystals. *Physical Review B*, 94(24):245115, 2016.
- [36] Stefan Feldkemper and Werner Weber. Generalized calculation of magnetic coupling constants for mott-hubbard insulators: Application to ferromagnetic cr compounds. *Physical Review B*, 57(13):7755, 1998.
- [37] Hans Ludwig Schläfer and Günter Gliemann. *Basic principles of ligand field theory*. Wiley-Interscience, 1969.
- [38] G Van der Laan and IW Kirkman. The 2p absorption spectra of 3d transition metal compounds in tetrahedral and octahedral symmetry. *Journal of Physics: Condensed Matter*, 4(16):4189, 1992.
- [39] JF Dillon Jr, H Kamimura, and JP Reineika. Magneto-optical studies of chromium tribromide. *Journal of Applied Physics*, 34(4):1240–1245, 1963.
- [40] Alejandro Molina-Sánchez, Gonçalo Catarina, Davide Sangalli, and Joaquin Fernandez-Rossier. Magneto-optical response of chromium trihalide monolayers: chemical trends. *Journal of Materials Chemistry C*, 8(26):8856–8863, 2020.
- [41] Michael A McGuire, Hemant Dixit, Valentino R Cooper, and Brian C Sales. Coupling of crystal structure and magnetism in the layered, ferromagnetic insulator CrI_3 . *Chemistry of Materials*, 27(2):612–620, 2015.
- [42] JF Dillon Jr and CE Olson. Magnetization, resonance, and optical properties of the ferromagnet CrI_3 . *Journal of Applied Physics*, 36(3):1259–1260, 1965.
- [43] Xiaopeng Liu, Dominik Legut, and Qianfan Zhang. Light-induced ultrafast enhancement of magnetic orders in monolayer CrX_3 . *The Journal of Physical Chemistry C*, 127(27):13398–13406, 2023.
- [44] Andrei L Tchougréeff and Richard Dronskowski. Nephelauxetic effect revisited. *International Journal of Quantum Chemistry*, 109(11):2606–2621, 2009.
- [45] YO Kvashnin, Anders Bergman, AI Lichtenstein, and MI Katsnelson. Relativistic exchange interactions in CrX_3 ($\text{X} = \text{Cl, Br, I}$) monolayers. *Physical Review B*, 102(11):115162, 2020.
- [46] Jun Miyawaki, Shigemasa Suga, Hidenori Fujiwara, Masato Urasaki, Hidekazu Ikeno, Hideharu Niwa, Hisao Kiuchi, and Yoshihisa Harada. Dzyaloshinskii-moriya interaction in $\alpha\text{-Fe}_2\text{O}_3$ measured by mag-

- netic circular dichroism in resonant inelastic soft x-ray scattering. *Physical Review B*, 96(21):214420, 2017.
- [47] Christian Schulz, Klaus Lieutenant, Jie Xiao, Tommy Hofmann, Deniz Wong, and Klaus Habicht. Characterization of the soft x-ray spectrometer peaxis at bessy ii. *Journal of Synchrotron Radiation*, 27(1):238–249, 2020.
- [48] M Grzeszczyk, S Acharya, D Pashov, Z Chen, K Vaklinova, M van Schilfgaarde, K Watanabe, T Taniguchi, KS Novoselov, MI Katsnelson, et al. Strongly correlated exciton-magnetization system for optical spin pumping in CrBr_3 and CrI_3 . *Advanced Materials*, 35(17):2209513, 2023.
- [49] Swagata Acharya, Dimitar Pashov, Alexander N Rudenko, Malte Rösner, Mark van Schilfgaarde, and Mikhail I Katsnelson. Excitons in bulk and layered chromium trihalides: from frenkel to the wannier-mott limit. *arXiv preprint arXiv:2110.08174*, 2021.
- [50] Yukito Tanabe and Satoru Sugano. On the absorption spectra of complex ions ii. *Journal of the Physical Society of Japan*, 9(5):766–779, 1954.